Materials Today Bio 32 (2025) 101693

Contents lists available at ScienceDirect

Materials Today Bio

journal homepage: www.journals.elsevier.com/materials-today-bio

Constructing J-aggregates of cyanine dye for NIR-II in vivo dynamic vascular imaging and long-term targeting of tumors

Jiaqi Zhou [a,1], Hao Li [a,1], Hui Li [e], Jiayi Ding [e], Zhong Du [c], Jiabao Xiong [d], Hongyang Yao [a], Xueliang Zhang [a], Nuernisha Alifu [a,d,f,*], Biao Dong [b,**]

[a] State Key Laboratory of Pathogenesis, Prevention and Treatment of High Incidence Diseases in Central Asia, School of Medical Engineering and Technology, Xinjiang Medical University, Urumqi, 830054, China
[b] State Key Laboratory on Integrated Optoelectronics, College of Electronic Science and Engineering, Jilin University, Changchun, 130012, China
[c] The First Affiliated Hospital, Xinjiang Medical University, Urumqi, 830011, China
[d] The Second Affiliated Hospital, Xinjiang Medical University, Urumqi, 830011, China
[e] Institute of Public Health, Xinjiang Medical University, Urumqi, 830011, China
[f] Engineering Research Center of Xinjiang and Central Asian Medicine Resources, Ministry of Education, Urumqi, 830054, China

ARTICLE INFO

Keywords:
IR-783
TMTP1
J-aggregates
Tumor targeting

ABSTRACT

Cyanine molecules with the second near-infrared (NIR-II) emission hold great potential for bioimaging owing to their great biocompatibility, but the scissor-like structure of these molecules poses a major bottleneck in obtaining efficient NIR-II fluorescence probes. Constructing J-aggregates represents a promising strategy for obtaining biomedical NIR-II emissive materials. However, achieving J-aggregates in cyanine dyes with large torsion angles between the heterocyclic rings poses a challenge. In this study, we introduced the guanidine of tumor molecular targeted peptide 1 (TMTP1) to increase steric hindrance of IR-783 and reduce the angle of IR-783 scissors. The near-coplanar structure of IR-783@peptide TMTP1 composite facilitates the formation of a novel J-aggregates (IR-783-LP-TMTP1) with super-stable effect for NIR-II in vivo dynamic vascular imaging and remarkable tumor targeting capability. The stable emission wavelength and high spatial resolution of J-aggregates was demonstrated for brain and ear vasculature bioimaging under 808 nm laser excitation. Additionally, J-aggregates exhibits robust tumor-targeting capability towards cervical tumors, indicating their potential in cervical cancer diagnosis. This work develops a molecular design strategy to construct bright NIR-II J-aggregates with super-stable and robust tumor-targeting properties and paving the way for improving bioimaging performance of similar molecules.

1. Introduction

Near-infrared fluorescence (NIR) imaging emerges as a promising role in disease diagnosis for early detection, offering high spatial and temporal resolution, sensitivity, and non-radioactivity [1–7]. In 2009, the discovery of the second near-infrared (NIR-II, 900–1700 nm) spectral window using single-walled carbon nanotubes (SWCNTs) marked a significant breakthrough [8–11]. Since then, a growing array of NIR-II

Abbreviations: NIR, near-infrared; SWCNTs, single-walled carbon nanotubes; ACQ, aggregation-caused quenching; TMTP1, tumor molecular targeted peptide 1; NPs, nanoparticles; NIR-I, near-infrared-I; NIR-II, near-infrared-II; TEM, transmission electron microscope; DLS, dynamic light scattering; OD, optical density; QY, quantum yield; NMR, nuclear magnetic resonance; DMSO, dimethyl sulfoxide; DFT, density functional theory; TD-DFT, time dependent density functional theory; HOMO, highest molecular orbitals; LUMO, lowest unoccupied molecular orbitals; FE, Frenkel exciton; PCM, polarizable continuum model; SBR, signal-to-background ratio; FWHM, full width at half maximum; SLN, sentinel lymph nodes; SPC, soya phosphatidylcholine; DMF, dimethylformamide; DMEM, dulbecco's modified eagle mediumE; PBS, phosphate-buffered saline; CCK-8, cell counting kit-8; FBS, fetal bovine serum; DI, deionized; FTIR, fourier infrared spectrometer; HeLa, human cervix carcinoma; ATCC, the American Type Culture Collection; WD, working distance.

* Corresponding author. State Key Laboratory of Pathogenesis, Prevention and Treatment of High Incidence Diseases in Central Asia, School of Medical Engineering and Technology, Xinjiang Medical University, Urumqi, 830054, China.
** Corresponding author.
E-mail addresses: nens_xjmu@126.com (N. Alifu), dongb@jlu.edu.cn (B. Dong).
[1] These authors contributed equally.

https://doi.org/10.1016/j.mtbio.2025.101693
Received 16 January 2025; Received in revised form 8 March 2025; Accepted 20 March 2025
Available online 27 March 2025

fluorophores, including inorganic quantum dots [12–14], rare earth doped nanoparticles [15–17], and cyanine dyes [18–22], have been harnessed for NIR fluorescence bioimaging. Among them, cyanine dyes have found widespread application in the biomedical field due to their superior biocompatibility [23–25]. These cyanine molecules's structural likeness, typified by ICG, IR-783, IR-820, FD-1080, characterized by two heterocycles with nitrogen/sulfur/oxygenand methicryl conjugated chains, results in a substantial conjugated system [26]. The limited steric hindrance between the heterocyclic structures at both ends renders them prone to intermolecular torsion in polar solvents, leading to suboptimal stacking and aggregation-caused quenching (ACQ) [27]. The advancement of such cyanine molecules is impeded by their unsatisfactory emission wavelength and ACQ in biological contexts. Consequently, simultaneously regulating the longer emission wavelength and anti-quenching ability of these molecules presents a significant challenge [28,29]. Furthermore, another common issue with these small molecules (including ICG, IR-806, IR-820, FD-1080, IRDye 800CW, etc.) lies in their tumor-targeting specificity [30,31]. Although they are easily metabolized, insufficient accumulation at tumor sites can also impact imaging effectiveness, limiting their broader biological applications.

Constructing J-aggregates represents a promising strategy to enhance photophysical properties and alleviate ACQ effect [32–34]. Studies have demonstrated the facile generation of J-aggregates in numerous planar molecules [35–37]. However, achieving J-aggregation in cyanine dyes with large π-conjugated structures remains a significant challenge. This difficulty arises from the positive charge located between the heterocyclic rings in cyanine dye molecules, which minimizes steric hindrance and promotes face-to-face stacking, leading to the formation of H-aggregates [38]. Various strategies have been explored to address these issues, including the regulation of hydrophilic/hydrophobic interactions and steric hindrance. For instance, Chen et al. developed an NIR-II fluorescence probe based on IR-140 and hollow mesoporous silica nanoparticles (HMSNs), leveraging hydrophilic/hydrophobic interactions to induce J-aggregation [39]. Similarly, Du et al. fabricated IR1061@HSA nanoparticles, where intermolecular rotation was restricted by hydrophilic/hydrophobic interactions to promote J-aggregate formation [40]. It is worth noting that solvent types can also influence hydrophilic/hydrophobic interactions, further impacting the formation of J-aggregates. Therefore, enhancing steric hindrance represents a promising avenue for facilitating J-aggregation. For example, Li et al. introduced a dodecyl(triphenyl)phosphonium cation (Pc) as the counterion for an anionic tricyanofuran-based trimethine, enabling the formation of supramolecular J-aggregates with enhanced photostability (C3T-Pc) [41]. To the best of our knowledge, due to the challenges in identifying suitable substituents, a strategy that simultaneously enhances steric hindrance to achieve J-aggregate formation and tumor-targeting capability in cyanine dyes has yet to be reported.

It is hypothesized that replacing the positive charge with a large cationic group may increase steric hindrance. Guanidine is a large-volume, positively charged organic group, also known as the R group of arginine, contributing to the high isoelectric point of arginine. The structural stability issue of such cyanine dyes may potentially be addressed by introducing a guanidine group. In addition, since arginine can serve as a residue in a targeting peptide containing arginine for such small molecules could simultaneously address both J-aggregate and tumor-targeting issues, which may be a significant strategy for the biological application of these molecules.

As a proof of concept, we selected a tumor molecular targeted peptide 1 (TMTP1, NVVRQ), featuring arginine as the last amino acid to introduce a larger positive charge from the guanidine group. A typical polymethine cyanine fluorophore, IR-783, was chosen as the research model, given its characteristic of having a positive Na^+ charge between its two heterocycles, which readily ionizes in polar solvents. To address the challenge of the direct connection between TMTP1 and free IR-783, we modified TMTP1 with DSPE-PEG-Maleimide and coated it with liposomes, obtaining a novel type of NIR-II J-aggregate fluorophore, IR-783-LP-TMTP1 nanoparticles (NPs), with super-stable effect for NIR-II *in vivo* dynamic vascular imaging and outstanding tumor targeting capability [42]. High spatial resolution of IR-783-LP-TMTP1 NPs was demonstrated for brain and ear vasculature bioimaging under 808 nm laser excitation. Additionally, IR-783-LP-TMTP1 NPs exhibits robust tumor-targeting capability towards cervical tumors with prolonged tumor retention time, indicating their potential in cervical cancer diagnosis (Scheme 1). Therefore, our molecular design strategy can construct bright NIR-II J-aggregates with super-stable and robust tumor-targeting properties and paving the way for improving bioimaging performance of similar molecules.

2. Experimental section

2.1. Materials

IR-783, DSPE-PEG-Maleimide and soya phosphatidylcholine (SPC) were all purchased from Aladdin Reagent Co., Ltd, China. Cholesterol was purchased from Solarbio Co., Ltd. TMTP1 and dimethylformamide (DMF) were purchased from Xi'an Ruixi Co., Ltd. Dulbecco's modified eagle mediumE (DMEM), phosphate-buffered saline (PBS), dimethyl sulfoxide (DMSO), tetrahydrofuran (THF), penicillin/streptomycin and trypsase were purchased from Shanghai MacLean Biochemical Co., Ltd. The cell counting kit-8 (CCK-8), 96-well cell culture plates, cell culture dishes and 15 mL centrifuge tube were purchased from Bio-sharp Co., Ltd. Fetal bovine serum (FBS) was purchased from Gibco Co., Ltd. Chloroform and deionized (DI) water was acquired from the central-lab of Xinjiang Medical University.

2.2. Instruments

A Shimadzu UV-3600i Plus UV–vis–NIR spectrophotometer was used to measure the absorption spectra of the samples (IR-783, IR-783-LP NPs and IR-783-LP-TMTP1 NPs). NIR fluorescence spectra of the samples (IR-783, IR-783-LP NPs and IR-783-LP-TMTP1 NPs) were recoroded by a Shinadzu RF-6000 fluorescence spectrophotometer. The zeta potential and diameter size distribution of the samples (IR-783, IR-783-LP NPs and IR-783-LP-TMTP1 NPs) were measured with a nanometer particle size potentiometer (NanoBrook 90Plus PALS, Brookhaven). The structure and morphology of IR-783-LP-TMTP1 NPs was characterized by transmission electron microscope (TEM) (JEM-1230, Japan). The toxicity of the samples (IR-783, IR-783-LP NPs and IR-783-LP-TMTP1 NPs) to human cervix carcinoma (HeLa) cells was determined by microplate reader (Thermo Fisher Instruments Co,.Ltd). The Fourier infrared spectroscopy (FTIR) of the samples (IR-783, IR-783-LP NPs and IR-783-LP-TMTP1 NPs) were tested by Fourier infrared spectrometer (VERTEX70 RAM II). The nuclear magnetic resonance (NMR) hydrogen spectrum of the sample (TMTP1, DSPE-PEG-Maleimide, IR-783 and IR-783-LP-TMTP1 NPs) were recorded by the NMR EFT-60 (60 MHz) and EFT-90 (90 MHz)(American Anasazi). NIR-I fluorescence images were captured by small animal imaging system (AniView100, Guangzhou Boluteng Biological Technology Co., Ltd, China.), under 745 nm excitation and 840 nm emission light. NIR-II fluorescence quantum yields (QYs) of the samples (IR-783, IR-783-LP NPs and IR-783-LP-TMTP1 NPs) in DI water were measured by steady state/transient fluorescence spectrometer (FLS980, Edinburgh Co., Ltd). The 808 nm semiconductor laser was purchased from Changchun Lishi Photoelectric Technology Co., Ltd. The commercial upright microscope, 3.3× objective lens and 900 nm, 1100 nm and 1200 nm filters was purchased from SOPTOP Co., Ltd. The 100× objective lens (Plan Apo NIR) was purchased from GRAND UNIFIED OPTICS Co., Ltd.

2.3. Cells cultures

The L929 cells, cervical normal cells (H8) and HeLa cells were

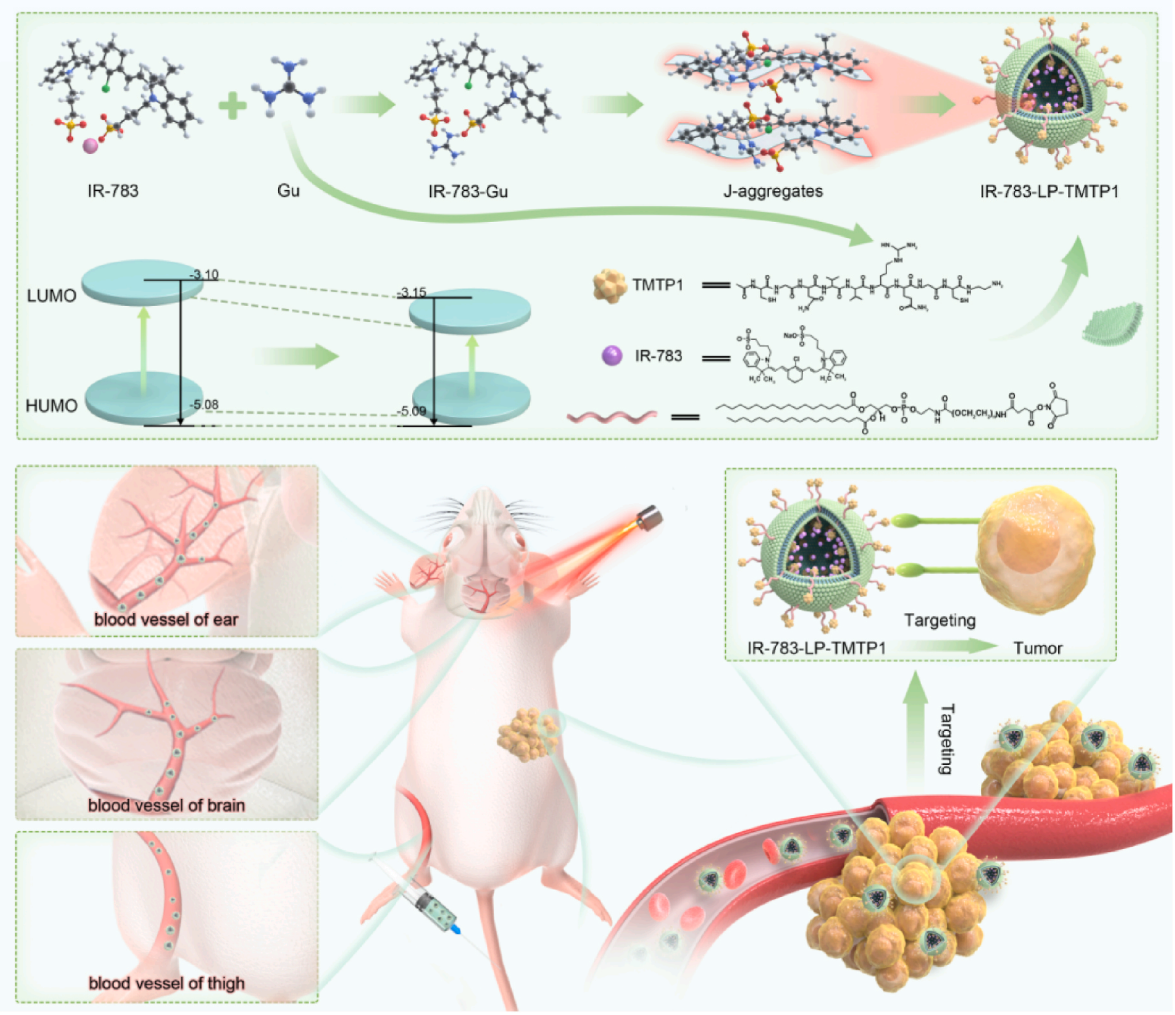

Scheme 1. Schematic illustration of synthesis process of J-aggregates, chemical and energy level structure, and application for *in vivo* NIR-II fluorescence imaging.

obtained from the Shanghai cell bank, and the cells were cultured in DMEM (91 %), FBS (8 %) and penicillin/streptomycin (1 %) at 37 °C and 5 % CO_2 humidified atmosphere.

2.4. Animals preparation

The animal tissue and model in this study were purchased from Vital River Laboratory in Beijing and the Animal Laboratory Center of Xinjiang Medical University. All animal experimental procedures were approved by the Ethics Committee of Animal Laboratory Studies of Xinjiang Medical University (IACUC-20211016-48).

2.5. Density functional theory calculations

The ground-state (S_0) geometries of structure-simplified IR-783 and IR-783-Gu (Gu stands for guanidine in TMTP1) were optimized at the B3LYP/6-31G(d,p) level with GD3GJ dispersion correction [42–45]. The polarizable continuum model (PCM) and GD3GJ dispersion correction were employed to take into account the effects of the solvents. Time dependent density functional theory (TD-DFT) was used to compute the excited state property of the dye molecule [46]. The highest occupied molecular orbitals (HOMOs) and lowest unoccupied molecular orbitals (LUMOs), absorption excitation energies of these molecules were obtained based on their optimized S_0 geometries. The emission excitation energies of these molecules were calculated based on their optimized S_1 geometries. All the calculations were performed using the Gaussian 16 software.

2.6. Preparation of IR-783-LP NPs

Firstly, 1 mg of IR-783 was dissolved in 1 mL of DI water to obtain an aqueous solution of IR-783. Then, 10 mg of SPC and 1 mg of cholesterol were added into the nightshade flask with containing 1 mL of chloroform. The mixture was then stirred with a magnetic stirrer at a speed of 1000 r min^{-1} for 24 h. After complete evaporation of chloroform, the bottom of the bottle form a film. Then the IR-783 aqueous solution was added to the bottle and perform ultrasonication for 15–20 min. The solution was filtered after ultrasonication to remove unpacked IR-783 and obtain an aqueous dispersion of IR-783-LP NPs.

2.7. Preparation of DSP-PEG-TMTP1 NPs

100 mg of DSPE-PEG-Maleimide was dissolved in 3 mL of DMF, and then the peptide TMTP1 was added into the solution. The reaction mixture was allowed to react for 12 h. Next, the reaction solution was transferred into a dialysis bag with a molecular weight cutoff of 1000 Da and dialyzed in pure water for 24 h. The collected dialysate was freeze-dried to obtain DSP-PEG-TMTP1 NPs.

2.8. Preparation of IR-783-LP-TMTP1 NPs

The SPC, cholesterol, IR-783, DSPE-PEG-TMTP1 were dissolved in 3

mL of chloroform, and evaporated into a film under reduced pressure in the sample bottle, then 2 mL of DI water was added. After ultrasound and liposome extruder (polycarbonate film, pore size 100 nm) treatment. The unsupported DSPE-PEG-TMTP1 NPs and IR-783 were removed by nanodialysis apparatus (polycarbonate membrane, pore size 30 nm). Finally, IR-783-LP-TMTP1 solution was obtained by adding deionized water at a constant volume of 10 mL.

2.9. Cytotoxicity analysis

The cytotoxicity of samples (IR-783, IR-783-LP NPs and IR-783-LP-TMTP1 NPs) to normal cells was evaluated by CCK-8 method. L929 cells were planted in 96-well cell plates, where each well in the experimental group contained 5×10^3 of cells and 100 μL of complete medium and incubated for 24 h. Samples (IR-783, IR-783-LP NPs and IR-783-LP-TMTP1 NPs) were dissolved in DMEM medium to form different concentrations (40 80 120 160 and 200 μg mL^{-1}) and then incubated different concentrations of complete medium with L929 cells for 24 h. Each concentration was set up with 5 compound pores, and the blank group did not contain cells in each hole, only complete media. After incubation for 24 h, 10 μL of CCK-8 indicator was added to each well, and then the 96-well plates were placed in the cell incubator for 2 h. Then the absorbance value of each hole was detected by enzyme-labeling assay, and the cell survival rate was calculated by CCK-8 standard method.

2.10. In vitro stability evaluation

The three capillary glass tubes filled with NPs at the same absorbance under 808 nm laser were put on a platform under the abovementioned NIR-II fluorescence microscopic system. NIR fluorescence intensity of the three capillary glass tubes for a longer period (1–7 days) and for a shorter period (30 min) under continuous laser irradiation at 808 nm (0.5 W cm^{-2}) was recorded.

2.11. In vitro fluorescence properties analysis

The same optical density of three samples were loaded in the capillary and imaged under the NIR-II fluorescence microscopy imaging system under 808 nm laser excitation. To test penetration depth in biological tissue of samples (IR-783, IR-783-LP NPs and IR-783-LP-TMTP1 NPs), bovine muscle and fat were selected to simulate biological tissue, capillary glass tubes to simulate human blood vessels 0.3 mm of beef muscle and fat were cutted respectively and covered with slide. Put these slide on the capillary, the NIR-II fluorescence microscopic images of tissue with different penetration depth were recorded under 808 nm laser irradiation.

2.12. QY analysis

The QYs of samples (IR-783 and IR-783-LP-TMTP1 NPs) in aqueous dispersion were measured by Hangzhou Research Interest Information Technology Co., LTD. The photoluminescence (PL) measurement of samples were carried out on a steaty state/transient fluorescence spectrometer (FLS980, Edinburgh Instruments Co., Ltd).

2.13. In vitro targeting specificity of IR-783-LP-TMTP1 NPs

Cervical normal cells (H8) and HeLa cells were tested for their specific detection capability using CLSM, staining with Hoechst-333342. H8 and HeLa cells were inoculated at 3×10^6 cells (80 μL) in the single petri dish and then cultured overnight.

2.14. Hemolysis test of IR-783-LP-TMTP1 NPs

Blood samples were collected from healthy BALB/c mice into heparinized tubes and centrifuged at 2700 rpm for 15 min to isolate red blood cells (RBCs). The collected RBCs were washed three times with 1 × PBS to prepare a 2 % RBC suspension. Subsequently, the RBC suspension were treated with IR-783-LP-TMTP1 NPs at concentrations of 20, 40, 60, 80, 100, 120, 140, 160 μg mL^{-1} in physiological saline for 2 h at 37 °C. DI water and physiological saline were used as positive and negative controls, respectively. Finally, 100 μL of the supernatant was collected and transferred to a 96-well plate. The optical density (OD) at 545 nm was measured using an enzyme-linked immunosorbent assay (ELISA) microplate reader.

2.15. In vivo pharamcokinetic of IR-783-LP-TMTP1 NPs

The in vivo pharamcokinetic of NPs was performed using the small animal imaging system (AniView100, Guangzhou Boluteng Biological Technology Co., Ltd, China.). The PBS (200 μL, control group) and IR-783-LP-TMTP1 NPs (200 μL, 1 mg mL^{-1}) in aqueous dispersion was intravenously injected into the female nude mice and the fluorescence signals were collected at various time points (5 min, 24 h, 48 h and 72 h) respectively. After 72 h, the mice were sacrificed, the dissected major organs were observed for ex vivo NIR fluorescence imaging.

2.16. Establishment of cervial tumor model

The HeLa cells was obtained from the American Type Culture Collection (ATCC). Firstly, place the cell complete medium, phosphate balance fluid and trypsin together in a 37 °C constant temperature water bath. Next, use a pipette to remove and discard the old culture medium in the HeLa cell culture dish. Then, draw up 3 mL of 1 × PBS and gently shake the dish to thoroughly wash away dead cells and metabolites. Afterwards, use the pipette to remove and discard the PBS from the dish, repeating this process 2–3 times. Next, 2 mL of trypsin was added to the petri dish, and the cell culture dish was placed back in the 5 % carbon dioxide cell incubator for 2 min. The petri dishes were then placed under a microscope to see whether the cells came off the dishes. If the cells are completely removed from the dish, digestion can be terminated. If it does not fall off, the digestion time can be properly prolonged. After the cells were completely removed from the petri dish, 4 mL of complete cell medium was added to the petri dish to terminate digestion. After mixing, 15 mL of cell suspension was transferred to a centrifuge tube. Put the centrifuge tube into the centrifuge with 1000 r min^{-1} for 5 min. Then, the supernatant is absorbed and discarded. Re-add 5 mL of cell complete medium into the 15 mL of centrifuge tube and mix the cells evenly to make cell suspension. Place the cover slip flat in the middle counting area of the hemocytometer, and inject cell suspension into the gap between the cover slip and counting chamber from the edge of the cover slip. Then, the counting chamber under a microscope was observed. The average value for each counting region was calculated, and multiply this value by 1×10^4 cells mL^{-1} to obtain the concentration of cell suspension. If the value is too high to count accurately, dilute the cell suspension accordingly and recount. 1×10^{-7} of HeLa cells were evenly mixed with 200 μL of phosphate solution. Then the back of nude mice was injected 1 mL of syringe into the right lower back of the mice. Next, the subcutaneous tumor volume was observed until grew up to 50 mm^3 for about 2 weeks.

2.17. In vivo NIR-I fluorescence imaging

The in vivo NIR-I fluorescence imaging was performed using the small animal imaging system (AniView100, Guangzhou Boluteng Biological Technology Co., Ltd, China.). The PBS (30 μL, control group) and IR-783-LP-TMTP1 NPs (30 μL, 1 mg mL^{-1}) in aqueous dispersion was intramuscularly injected into the female nude mice and the fluorescence signals were collected at various time points (0 h, 0.5 h, 11 d and 18 d) respectively. After 18 d, the mice were sacrificed, the dissected SLN and tumor were observed for ex vivo NIR fluorescence imaging.

2.18. Optical setup for NIR-II whole body/microscopic fluorescence imaging system

NIR-II fluorescence microscopic system was built by using a commercial upright microscope (NIR-II-MS, SOPTOP) equipped with InGaAs camara (640 × 512 pixels) and an 808 nm laser beam as the excitation light source. The NIR-II fluorescence signals were collected through the same objective (SOPTOP, 3.3×, Working distance (WD) = 42.3) and then passed through a long-pass filter to eliminate any reflected excitation light. Imaging process were eventually recorded by the InGaAs camera.

2.19. In vivo NIR-II fluorescence microscopic imaging

In order to detect the fine brain vasculature under through-skull, the mice were anesthetized and fixed on a platform to ensure that their heads was irremovably. The head skin of the female nude mice were removed to expose the skull through surgery. At the time of imaging, then 200 μL of PBS (control group) and IR-783-LP-TMTP1(1 mg mL^{-1}, experimental group) was injected into the female nude mice through the tail vein (all the microscopic imaging like ear blood vessel and thigh vascular were carried out in this way unless mentioned especially). The mouse remained on the heating pad to maintain a liveable body temperature at 37 °C throughout surgery and imaging process.

2.20. Calculation of cerebral blood flow velocity

Cerebral blood flow signal were eventually recorded by the electronic-cooling InGaAs camera by using 100× objective. An exposure time of the camera was set to 50 ms by using InGaAs Camera Controller software. NIR-II fluorescence image sequences were captured at a frame rate of 40 ms (25 fps). Considering the low contrast in the video, we use image subtraction to calculate blood flow velocity in cerebral vessels. Disassemble the video into pictures one by one, find a continuous picture, subtract the first picture from the last picture in turn, and get the grayscale image. A series of grayscale were multiplied by 4 to obtain binary images of blood flow changes over time. All the imaging calculations were performed using the Matlab 2022 software.

2.21. In vivo and in vitro tumor targeting fluorescence imaging

PBS (200 μL, control group) and IR-783-LP-TMTP1 (200 μL, 1 mg mL^{-1}, experimental group) were intravenously injected into tumor-bearing nude mouse and imaged under aforementioned whole-body NIR-II fluorenscence imaging system at various time points (0 h, 24 h, 48 h and 72 h). The mouse were sacrificed after 72 h post-injection, the marjor organs (heart, liver, spleen, kidneys) and tumor were taken and observed for ex vivo NIR-II fluorescence imaging. The tumor tissue was sliced (slice thickness = 0.5 mm), and the distribution of IR-783-LP-TMTP1 NPs in each tumor slice was observed under NIR-II fluorescence microscopic system (808 nm laser irradiation). The fluorescence signal of tumor slice was recorded using InGaAs camera with 3.3× objective lens. Because the size of each tumor slice was larger than the field of view, multiple images per slice were collected via the 3.3× objective block-scanned the whole slice (3 mm × 4 mm) with a step size of 0.1–0.3 mm. The multiple images per slice were stitched to perform a large image by using the PTGui Pro software.

2.22. Evaluation of nanoparticles retentive ability in tumors

To test the retention capacity of nanoparticles in tumors, PBS (30 μL, control group), IR-783 (30 μL, 1 mg mL^{-1}) and IR-783-LP-TMTP1 NPs (30 μL, 1 mg mL^{-1}) were intratumoral injected into cervical tumour-bearing nude mice and imaged at various time points (1 d, 3 d, 5 d, and 7 d). Then, the time of strongest fluorescence signal was recorded under the small animal imaging system with 745 nm excitation and 840 nm emission light.

3. Result and discussion

3.1. Photophysical properties

DSPE-PEG-TMTP1 was used to coat liposome-bound IR-783, resulting in the synthesis of a novel type of NIR-II fluorescence probe, IR-783-LP-TMTP1 NPs. DEPE-PEG-TMTP1 was prepared by coupling the thiol group (-SH) of TMTP1 to the maleimide group of DSPE-PEG-Maleimide (Fig. SI 1). The successful synthesis of DSPE-PEG-TMTP1 was confirmed by observing the characteristic peak of TMTP1 at 7.7 ppm in the nuclear magnetic hydrogen spectrum (Fig. SI 2). Characterization of IR-783, IR-783-LP NPs and IR-783-LP-TMTP1 NPs is conducted to explore their photophysical properties. The morphology of the IR-783-LP-TMTP1 NPs was examined by TEM, revealing a smooth spherical surface with an average diameter of approximately 100 nm (Fig. 1A; Fig. SI 3). Additionally, due to the presence of hydration layer surrounding the IR-783-LP-TMTP1 NPs, the particle size of NPs was measured to be approximately 108 nm by dynamic light scattering (DLS) (Fig. 1B). Furthermore, the low surface potential also indicates strong repulsive forces between particles of the same charge, IR-783-LP-TMTP1 NPs exhibited a zeta potential of −30.5 mV (Fig. 1C), demonstrating robust colloidal stability and biological compatibility. Subsequently, the optical properties was further studied, as shown in Fig. 1D–E. The absorption and emission wavelengths of IR-783-LP-TMTP1 NPs red-shifted by approximately about 21 nm compared with IR-783 and IR-783-LP NPs in DI water. The NMR hydrogen spectrum of IR-783-LP-TMTP1 NPs comfirmed that IR-783 has been successfully biomodified by TMTP1 (Fig. SI 4). To better understand the aggregate behavior of IR-783-LP-TMTP1 NPs, we explored the change of absorption of IR-783-LP-TMTP1 NPs in tetrahydrofuran (THF) volume fraction (*fw*). The absorption peak of IR-783-LP-TMTP1 NPs redshifts from 780 to 796 nm when the *fw* decreases from 80 % to 0 %, which means IR-783-LP-TMTP1 NPs forms ordered aggregate in DI water (Fig. SI 5). Especially, the emission at the same OD of IR-783-LP-TMTP1 NPs is efficiently enhanced by ≈ 1 times after forming J-aggregates. The QYs of monomer and J-aggregates are 0.64 % and 1.35 % respectively (Fig. SI 6). Such red-shifted absorption and emission of IR-783-LP-TMTP1 NPs could provide deep tissue penetration and improved bioimaging performance for *in vivo* applications.

The FTIR analysis was conducted to comfirm the conversion of IR-783 during the reaction process. Upon reacting with DSPE-PEG-TMTP1, several distinct peaks emerged in the spectrum in comparison to IR-783 alone (Fig. 1F). Notably, absorption peaks observed at 3010 cm^{-1} can be ascribed to the stretching vibration of unsaturated C-H bonds. Furthermore, a new absorption peak appeared at 1070 cm^{-1}, associated with the bending vibration of the S-O bond following TMTP1 modification, implying the substitution of positive charge Na^{+} with the guanidine group. Remarkably, all these bands exhibited a red-shift suggesting that the potential energy state of IR-783-LP-TMTP1 NPs was lower than that of IR-783. The chemical shift was observed in the guanidine group of TMTP1, moving from 7.65 ppm to 7.74 ppm in the NMR hydrogen spectrum of IR-783-LP-TMTP1 NPs. Combined with FTIR analysis, we can infer that the guanidine group may interact with IR-783 through eletrostatic adsorption (Fig. SI 4).

Impressively, the NIR-II fluorescence intensity of IR-783-LP-TMTP1 NPs remained at 99 % of its initial value after 30 min of continuous laser irradiation, indicating remarkable photostability (Fig. 1G). Additionally, IR-783-LP-TMTP1 maintained a robust fluorescence signal compared to IR-783 for 7 d (Fig. 1H), proving the stable J-type aggregation. This great photostability underscore the potential of IR-783-LP-TMTP1 NPs for NIR-II fluorescence bioimaging with the extended in vivo circulation time. The result indicated that the TMTP1 enables to regulate the arrangement of IR-783 molecules and restrict intermolecular rotation of IR-783, thereby enhancing fluorescence efficiency and

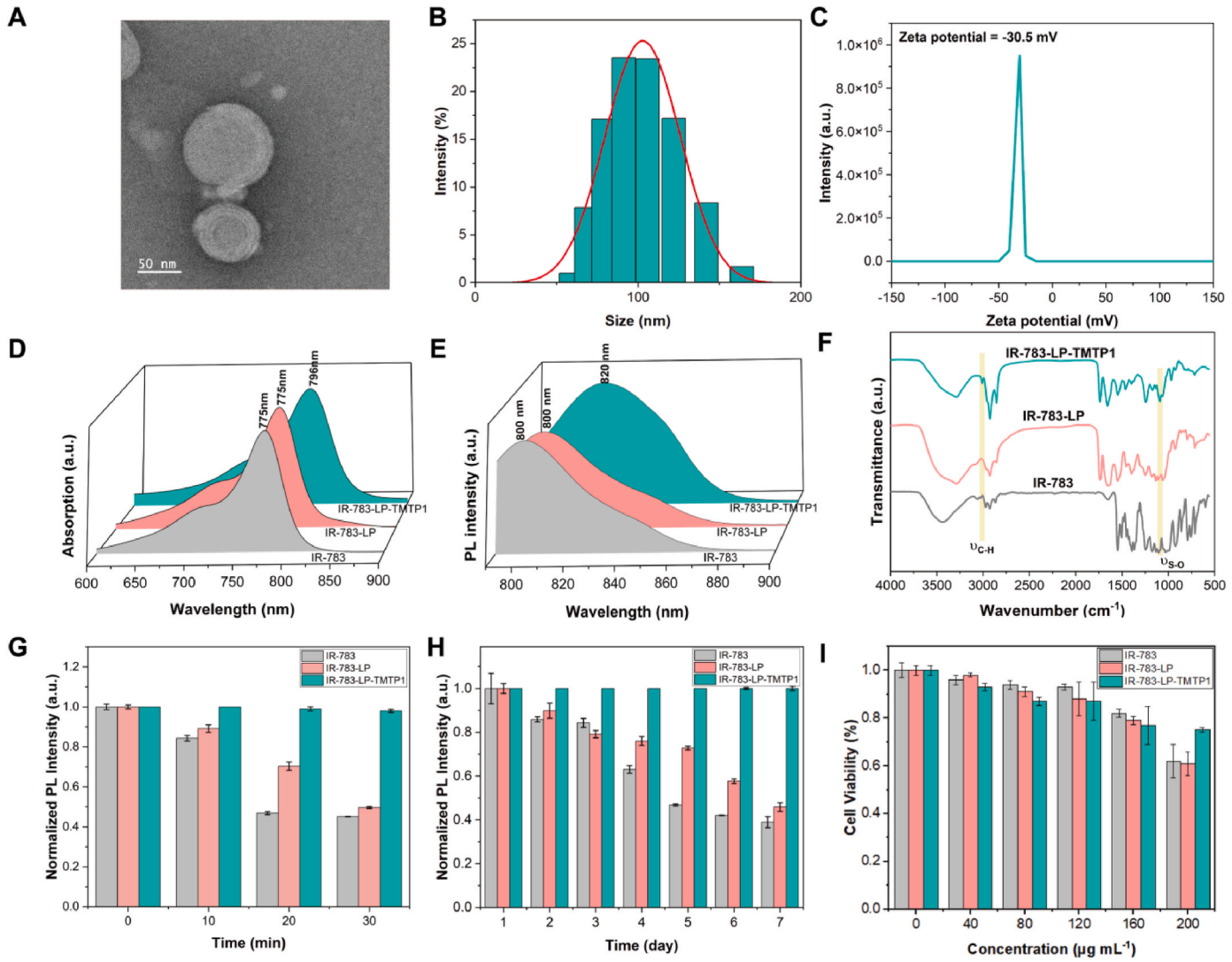

Fig. 1. Characterization of IR-783-LP-TMTP1 NPs. (A) TEM image of IR-783-LP-TMTP1 NPs in aqueous dispersion. Scale bar = 50 nm. (B) The particle size distribution of IR-783-LP-TMTP1 NPs in aqueous dispersion measured by DLS with a PDI of 0.18. (C) Zeta potential of IR-783-LP-TMTP1 NPs in aqueous dispersion. (D) Absorption spectrum of IR-783 (gray area), IR-783-LP (pink area) and IR-783-LP-TMTP1 (green area) in aqueous dispersion. (E) Fluorescence spectra of IR-783 (gray area), IR-783-LP (pink area) and IR-783-LP-TMTP1 (green area) in aqueous dispersion. (F) FTIR of IR-783, IR-783-LP and IR-783-LP-TMTP1. (G) Photostability of IR-783 (gray box), IR-783-LP (pink box) and IR-783-LP-TMTP1(green box) in aqueous dispersion as a function of time, under 808 nm continuous laser irradiation. Power = 50 mW. (H) Long-term photostability of IR-783 (gray box), IR-783-LP (pink box) and IR-783-LP-TMTP1 (green box) in aqueous dispersion for 7 days under 808 nm. power = 50 mW. (I) The potential cytotoxicity of IR-783 (gray box), IR-783-LP NPs (pink box) and IR-783-LP-TMTP1 NPs (green box) at different tested concentrations.

stability compared to IR-783 and IR-783-LP.

To further evaluate the biocompatibility of IR-783 and the NPs, the potential cytotoxicity and hemolysis rate were analyzed. In the CCK-8 experiment, as the concentration of the three samples increased, the survival rate of L929 cells gradually decreased (Fig. 1I). Treatment with IR-783-LP-TMTP1 NPs resulted in over 80 % cell survival at the tested concentrations. In the hemolysis experiment, the concentration of IR-783-LP-TMTP1 NPs increased will resulted in a rise of hemolysis percentage, which remained within the normal range (<5 %) (Fig. SI 7). The results of CCK-8 and hemolysis test suggested the low cytotoxicity and superior biocompatibility of IR-783-LP-TMTP1 NPs are suitable for NIR-II fluorescence in vivo bioimaging.

3.2. Synthesis and characterization of IR-783-LP-TMTP1

To further illustrate the effect of guanidine group in TMTP1 on the photophysical properties of IR-783, we performed density functional theory (DFT) calculations at the B3LYP/6-31G(d,p) level with GD3GJ dispersion correction. DFT calculations were performed to identify the optimized ground state (S_0) geometries of IR-783 (shown in Fig. 2A). As with most cyanine dyes molecules, IR-783 could be presented as a scissor-like structure. The backbone composed of two indolenine groups with vinylene bonds between them is regarded as scissor handle, while the butane-sulfonate chains extending from indolenine are considered to be scissor blades. The molecular adopt a positive charge center Na^+ with the scissors opening angle of about 34.4°, resulting the dihedral angle of two indolenine groups above 57.8°. To redshift the emission of organinc dyes, the widely explored strategy will be extend the length of conjugate chain, and a nearly coplanar structure is beneficial for enhancing the fluorescence properties. It suggests that replacing Na^+ with a positively charged guanidine group in IR-783 will decrease the opening angle of the butane-sulfonate chains and flatten the conjugated indolenines, thereby potentially enhancing NIR-II imaging quality. DFT calculations were further conducted using Gaussian 09 with identical parameters to those used for IR-783 to determine the structural configuration and electronic properties of the candidates. As anticipated, the planar

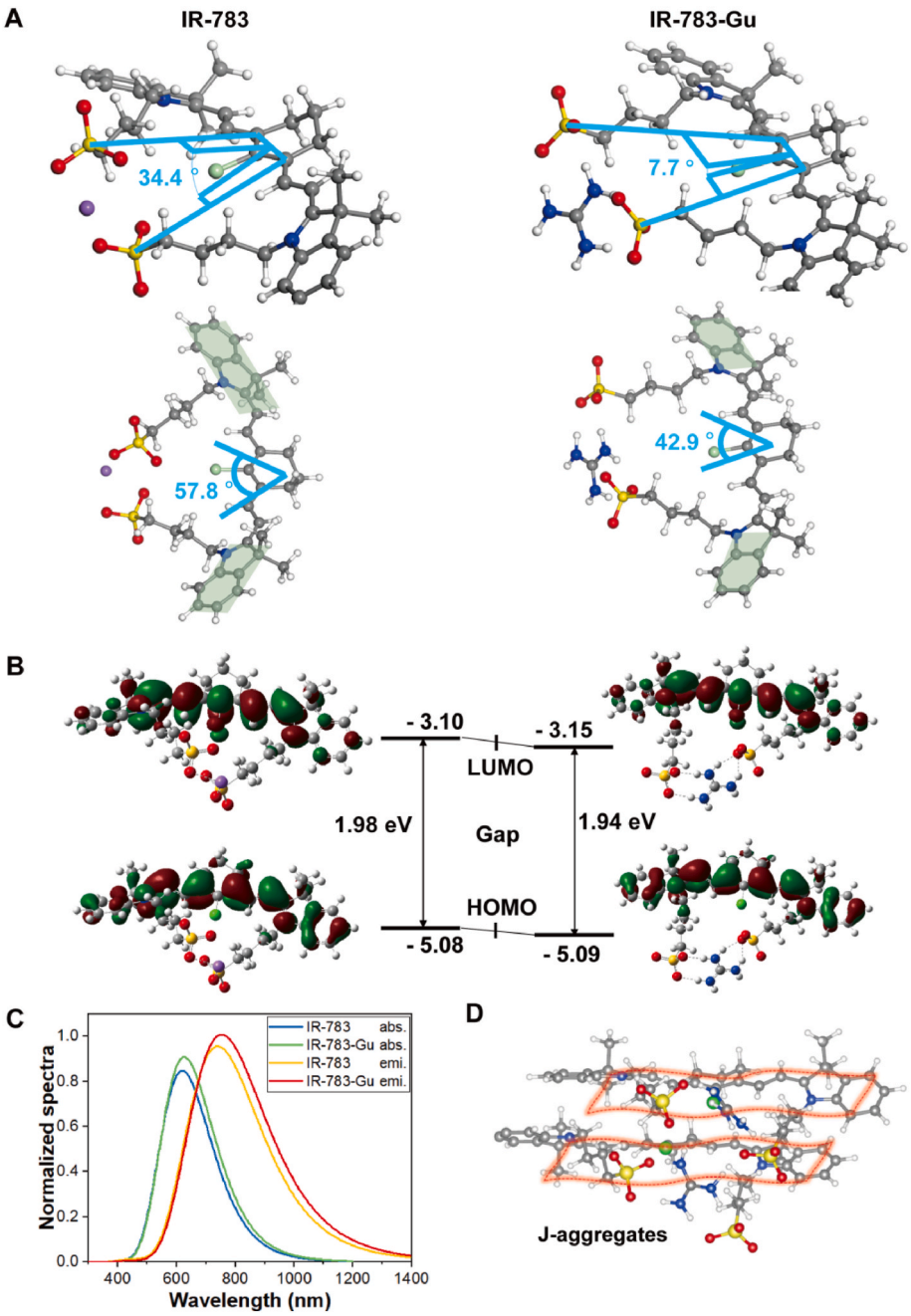

Fig. 2. Chemical structures and theoretical calculation results of IR-783 and IR-783-Gu. (A) Optimized S_0 geometries. (B) Illustration of the frontier molecular orbitals (LUMOs and HOMOs). (C) Calculated absorption and emission spectra of IR-783 and IR-783-Gu. (D) Schematic diagram of IR-783-Gu J-aggregates.

guanidine group was situated at the mouth of the scissors. The optimized ground state (S_0) geometries of guanidine-substituted IR-783 (IR-783-Gu) revealed a reduced scissor opening angle of 7.7°, significantly decreased the dihedral angles down to 42.9° between the two indolenines. This flatter planar structure is beneficial for enhancing NIR-II quality.

The HOMOs and LUMOs of both molecules are illustrated in Fig. 2B. The HOMO and LUMO of both molecules are delocalized along the indolenine groups backbone, revealing an excellent π–π* transition. The energy gap between HOMO and LUMO are 1.98 eV and 1.94 eV for IR-783 and IR-783-Gu, respectively, which is beneficial for absorbance in the longer wavelength region, as well as the small energy gap of IR-783-Gu also indicates a red-shifted absorption. The absorption and emission spectra of IR-783 and IR-783-Gu under aqueous solution conditions (Fig. 2C) were calculated. Owing to the same indolenine groups backbone, they exhibit similar absorption and emission spectra. Compared to IR-783, IR-783-Gu exhibits 6 nm and 13 nm of red-shifted absorption peak and emission peak, respectively. Furthermore, both the absorption and emission spectra of IR-783-Gu show a slight increase in intensity coefficient compared to those of IR-783. These results from electronic configurations demonstrate the viability of the presented molecular design strategy.

Furthermore, the assembly of two IR-783-Gu molecules is shown in Fig. 2D. It is notable that the neighboring IR-783-Gu molecules showed clear slipping with a distance of ~2.8 Å. The intermolecular distance was approximately 3.7 Å, confirming its π–π stacking character. Additionally, the slip angle was calculated to be around 30°. According to the Frenkel exciton (FE) model established by Kasha' team [47], a slip angle (θ) smaller than the critical value of 54.7° favors the formation of J-aggregates. These findings suggest that regulating the arrangement of

IR-783 molecules by guanidine group enables the efficient formation of long-wave stable J-aggregates in water.

3.3. Analysis of deep-tissue in vitro NIR-II fluorescence property

Inspired by the excellent fluorescence of IR-783-LP-TMTP1 NPs, the deep-tissue in vitro NIR-II fluorescence imaging performance was investigated under 808 nm laser. The samples (IR-783, IR-783-LP NPs and IR-783-LP-TMTP1 NPs) were prepared to the same OD at 808 nm and loaded in the capillary for imaging under the NIR-II fluorescence microscopic imaging system with 808 nm laser irradiation. To study the NIR-II fluorescence penetration ability of IR-783-LP-TMTP1 NPs in deep biological tissue, bovine muscle and fat of varying thicknesses were selected to simulate. The experimental process was shown in Fig. 3A.

0.3 mm of beef muscle and 0.3 mm fat were used and put on capilary glass tube which filled with samples (IR-783, IR-783-LP NPs and IR-783-LP-TMTP1 NPs) in aqueous dispersion respectively. The NIR-II fluorescence microscopic images of tissue with different penetration depth were recorded under 808 nm laser irradiation (the capillary glass tubes were IR-783, IR-783-LP NPs and IR-783-LP-TMTP1 NPs from left to right) in Fig. 3B. Fig. 3C displays the fluorescence intensity distribution corresponding to the images in Fig. 3B, while Fig. 3D presents a quantitative analysis of NIR-II fluorescence intensity for three samples under varying tissue thickness, using the same light irradiation and experimental conditions. The IR-783-LP-TMTP1 NPs exhibit significantly stronger fluorescence intensity and sharper imaging boundaries compared to IR-783 and IR-783-LP NPs. This enhancement is attributed to the guanidine group of TMTP1, which increases the steric hindrance of IR-783 and promotes the formation of stable J-aggregates with a near-coplanar structure in DI water. To further investigate the imaging performance, the signal-to-background (SBR) of the fluorescence images in Fig. 3B was analyzed in detail. As shown in Fig. 3E, the IR-783-LP-TMTP1 NPs achieve an SBR of 26 in the absence of tissue, outperforming IR-783 (14) and IR-783-LP NPs (17). When covered with 0.3

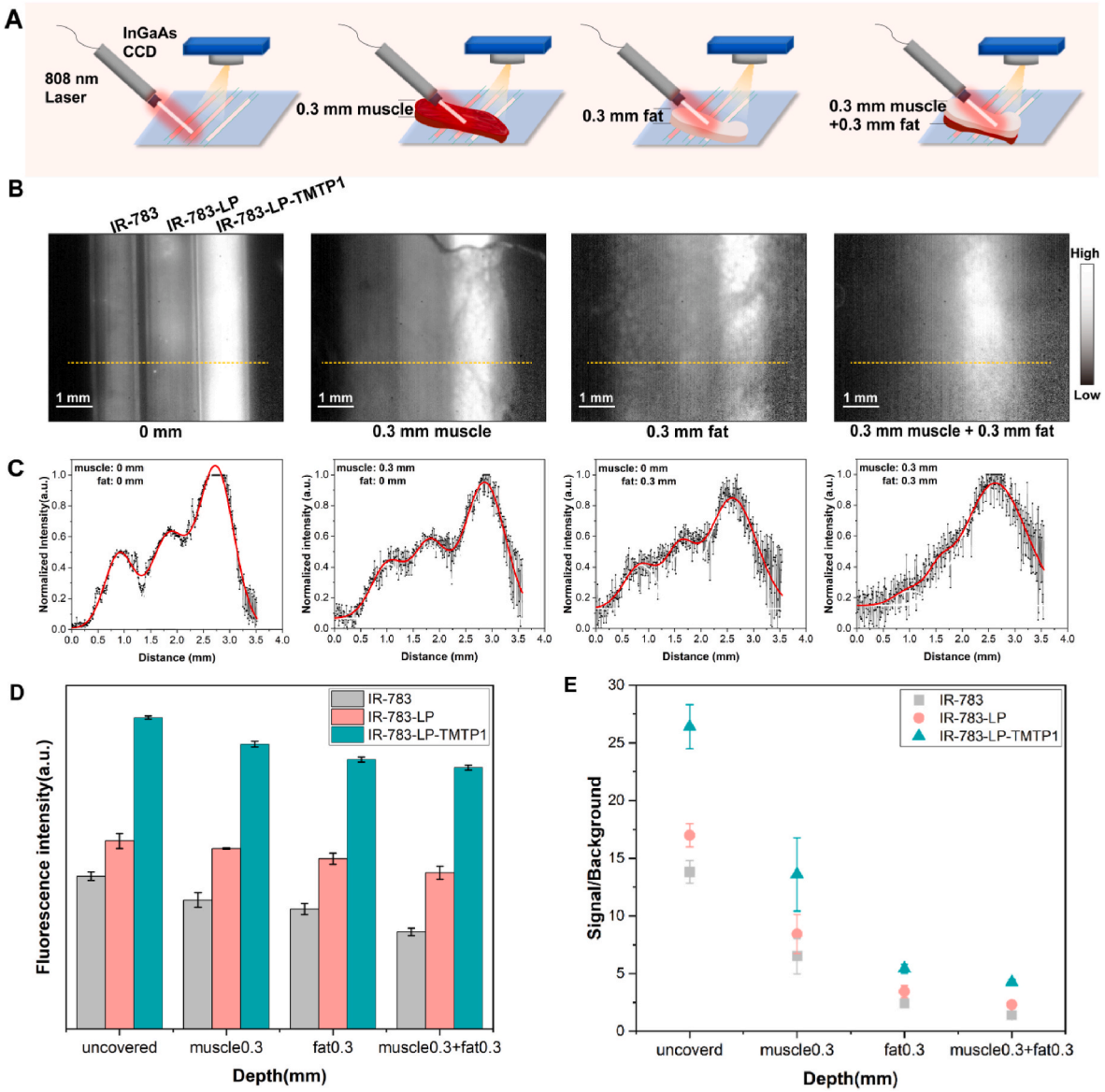

Fig. 3. Penetration depth in biological tissue. (A) The diagram of penetration depth of the three materials in different tissues. The three materials are IR-783, IR-783-LP NPs and IR-783-LP-TMTP1 NPs from left to right. (B) Glass capillaries were filled with IR-783, IR-783-LP NPs and IR-783-LP-TMTP1 NPs with no tissue covered; covering 0.3 mm of muscle tissue; covering 0.3 mm of adipose tissue; covering 0.3 mm of muscle and 0.3 mm of adipose tissue under 808 nm laser excitation. (C) The fluorescence intensity distribution corresponding to B. (D) The fluorescence intensity of the IR-783 (gray box), IR-783-LP NPs (pink box) and IR-783-LP-TMTP1 NPs (green box) at different tissue depths. (E) The SBR of IR-783,IR-783-LP and IR-783-LP-TMTP1 under different tissue depths.

mm of muscle tissue, the SBR of IR-783-LP-TMTP1 NPs remains as high as 14, compared to 6.5 for IR-783 and 8 for IR-783-LP NPs. Under 0.3 mm of adipose tissue, the SBR of IR-783-LP-TMTP1 NPs decreases to 5.5, still significantly higher than IR-783 (2.4) and IR-783-LP MPs (3.4). Even when both 0.3 mm muscle and adipose tissue are layered together, the SBR of IR-783-LP-TMTP1 NPs remains at 4.3, whereas the SBRs of IR-783 and IR-783-LP NPs drop to 1.4 and 2.3, respectively. As shown in Fig. SI 8, the intralipid was used to simulate tissues to evaluate the penetration ability of IR-783-LP-TMTP1 NPs and IR-783. IR-783-LP-TMTP1 NPs showed brighter fluorescence and clearer imaging boundaries than IR-783. These findings collectively demonstrate that IR-783-LP-TMTP1 NPs achieve superior tissue penetration depth and maintain higher SBR values, establishing their potential as an ideal NIR-II fluorescent probe for in vivo imaging applications. The enhanced performance is a direct result of the innovative molecular design that optimizes steric effects and stabilizes the J-aggregate structure. Encouraged by these results, we hypothesize that similar cyanine dyes (e.g., ICG, IR-808,IR-820, and FD-1080) could benefit from this

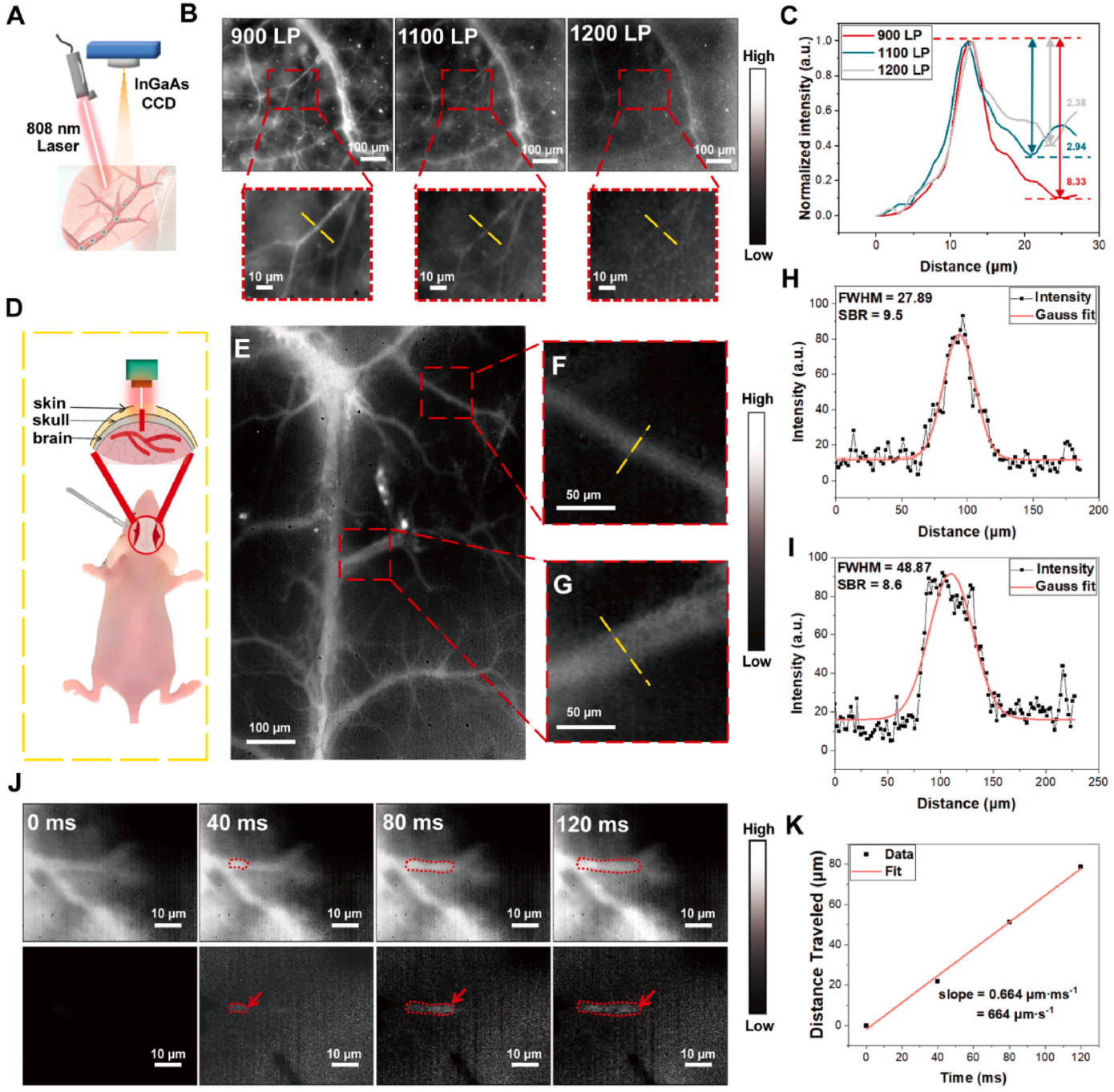

Fig. 4. In vivo NIR-II fluorescence microimaging of the mouse. (A) Schematic diagram of a mouse ear vessel. (B) The fluorescence images in the same ear blood vessels with 900 nm, 1100 nm and 1200 nm LP. Cross-sectional fluorescence intensity profiles along the yellow dotted lines of the blood vessel in ear. (C) The SBR of 900 LP,1100 LP and 1200 LP. (D) Schematic diagram of a mouse cerebral vessel by using NIR-II fluorescence imaging through the skull. (E) NIR-II fluorescence microscopic cerebrovascular imaging of a mouse for hemodynamics study. Cross-sectional fluorescence intensity profiles along the yellow dotted lines of the blood vessel in (F–G), corresponding the FWHM analysis in (H–J). (J) The different time points was tracked in a cerebral vessel (diameter ≈ 4.75 μm). Objective:100×. Exposure time: 50 ms. (K) The average blood velocity in mouse cerebral vessels.

molecular design strategy, potentially enhancing their photophysical properties and expanding their applications in NIR-II imaging. This hypothesis will be rigorously validated in subsequent experiments.

3.4. In vivo NIR-II fluorescence microscopic imaging

As the IR-783-LP-TMTP1 NPs have excellent stability and higher tissue peneration depth, blood vessel imaging is conducted to evaluate the in vivo NIR-II fluorescence imaging performance using an InGaAs detector with a 808 nm laser as the excitation.

The in vivo NIR-II fluorescence microscopic imaging ability of IR-783-LP-TMTP1 NPs was studied under different imaging windows (900 nm, 1100 nm and 1200 nm) via in vivo brain, ear blood and legs vessels of mice. NIR-II fluorescence microscopic images with high spatial resolution were obtained after the injection of IR-783-LP-TMTP1 NPs under 808 nm laser irradiation (Fig. 4A). As shown in Fig. 4B, the small ear blood vessels in mouse can be visualized more brighter under 900 nm window (900 nm long pass filter, 900–1700 nm) than other two windows (1100 nm and 1200 nm long pass filter). Although as the wavelength increases, the NIR-II microscopic fluorescence images becomes more clearer. However, considering the brightness and clarity simultaneously, in order to achieve the best imaging quality, we chosed the 900 nm window for NIR-II fluorescence microscopic imaging. To gain more comprehensive understanding for the NIR-II fluorescence microscopic images, the SBRs were analyzed by plotting cross-sectional intensity of the same small ear blood vessels (the yellow dotted line in the red square). The small vessels of the ear in 900 nm fluorescence image showed the best SBR of 8.33 while the same vessels possessed the SBRs of 2.94 and 2.38 in 1100 nm and 1200 nm windows, respectively (Fig. 4C). The same experimental process was repeated on the thigh blood vessels (Fig. SI 9A) and sentinel lymph node (SLN) (Fig. SI 9B) of the mice, and the same experimental results were obtained, imaging at 900 nm offers the highest spatial resolution.

The NIR-II fluorescence imaging can also be used to guide through-skull cerebral vessels imaging in living mice for dianosing the abnormalities of intracranial vascular. The injected mice were imaged under NIR-II fluorescence microscope with 900 nm long-pass filter under 808 nm laser irradiation (Fig. 4D). Because the size of cranial window was larger than the field of view, multiple images of cerebal vessels were collected via the 3.3× objective block-scanned the whole brain (diameter = 15 mm) with a step size of 1–3 mm. The multiple images of cerebal vessels were stitched to perform a full cerebrovascular image (Fig. 4E) by using the PTGui Pro software. The Gaussian-fitted full width at half maximum (FWHM) of several blood vessels (Fig. 4F and G) were analyzed, which indicated a diameter of 28.42 μm and 48.56 μm, respectively (Fig. 4H and I). The control group (PBS, 200 μL) showed no fluorescence signal, illustrating the J-type of IR-783-LP-TMTP1 NPs with enhanced photoluminescent enables clearly distinguish the signal between the target and background regions.

Moreover, the hemodynamic characteris of the mouse brain was assessed. We have video footage of blood flow in nude mouse with NIR-II fluorescence microscope under 100× objective. An exposure time of the camera was set to 50 ms by using InGaAs Camera Controller software. NIR-II fluorescence microscopic image sequences were captured at a frame rate of 40 ms (25 fps). The real-time video of brain blood flowing in NIR-II fluorescence images has been acquired after the tail vein injection of IR-783-LP-TMTP1 NPs (**Video S1**). Considering the low contrast in the video, the vascular images were enhanced at different time points by using image subtraction to facilitate calculate blood flow velocity in cerebral vessels [48]. Then a series of binary images corresponding to the changes of blood flow over time (Fig. 4J at the bottom) were obtained. All image processing operations were calculated by using the Matlab2022 software. By tracking the location of blood flow changes in a blood capillary in each binary image, we measured the average blood velocity to be ~664 μm s^{-1} in mouse cerebral vessels and calculated the volume blood flow (diameter ≈ 4.75 μm) of 0.297 μL min^{-1}. The results align well with previous studies (0.2–20,000 μm s^{-1}) (Fig. 4K) [49–51], comfirming that the J-aggregates formed by IR-783-LP-TMTP1 NPs maintain a stable emission wavelength under continuous 808 nm laser irradiation. This stability can be attributed to the guanidine group in TMTP1, which restricts the intramolecular rotation of IR-783, significantly enhancing its anti-quenching capability. Such properties greatly improve the dynamic monitoring performance of cyanine dyes, making IR-783-LP-TMTP1 NPs particularly promising for near-infrared biological real-time imaging. These characteristics underscore their potential to advance the sensitivity and reliability of imaging techniques in biomedical applications, particularly where long-term and precise visualization are required.

3.5. In vivo tumor targeting performance evaluation

TMTP1 is one of an ideal peptide which could target the cervical tumor. The IR-783-LP-TMTP1 NPs exhibited better cellular uptake by cervial cells (Hela) compared with IR-783 at the same concentration (Fig. SI 11). To analyze the in vivo tumor targeting performance of the IR-783-LP-TMTP1 NPs, the female nude mice were stochastic separated into two groups (n = 3 per group) to established the cervical tumor model. The 200 μL of IR-783-LP-TMTP1 (1 mg mL^{-1}) and PBS (control group) were intravenously injected into the tumor bearing-nude mouse and imaged under the NIR-II fluorescence imaging system. Then, the fluorescence signals were captured at different time points. The NIR-II fluorescence signals of IR-783-LP-TMTP1 NPs were observed in the site of tumor at 24 h post-injection (Fig. 5A). As time lapses, the NIR-II fluorescence intensity of IR-783-LP-TMTP1 NPs at the tumor sites gradually increased and reached the maximum at 72 th h (Fig. 5B; Fig. SI 12)). After 72 h, the mouse was sacrified. The tumor tissue and main organs were taken for in vitro imaging. Due to the targeting capability of TMTP1 towards the HeLa cells and the hydrodynamic diameter (HD) of IR-783-LP-TMTP1 NPs, the intense fluorescence signals was observed from the tumor site. Some fluorescence signals were also observed from the liver and spleen due to the engulfment of NPs by the mononuclear phagocyte system of the liver and spleen. Additionally, the kidneys are responsible for filtering and excreting small molecules. The fluorescent dye or its metabolites may be filtered through the glomeruli and accumulated in the renal tubules, leading to fluorescence signals. Fig. SI 10 further indicated the liver and kidney metabolic system are the main pathway for the clearance of the NPs from the body (Fig. 5C; Fig SI 10).

To assess the tumor penetration capability of IR-783-LP-TMTP1 NPs, NIR-II imaging was conducted on the tumor slice (slice thickness = 0.5 mm) (Fig. 5D), and the distribution of IR-783-LP-TMTP1 NPs in each tumor slice was observed under NIR-II fluorescence microscopic system (808 nm laser irradiation) with 3.3× objective lens. Fig. 5E showed that the fluorescence signal gradually decreased from the tumor margin to the interior. The cross-sectional fluorescence intensity profiles and Gaussian fits along a red-dashed line on the tumor section in Fig. 5F. The results indicated that IR-783-LP-TMTP1 gathered at the outer edge of the tumor, and the amount of IR-783-LP-TMTP1 entered the tumor interior was relatively small, which confirmed that NPs exhibits significant penetration ability into the central part of the tumor.

To further demonstrate the effectiveness of our molecular design strategy in enhancing the tumor targeting of cyanine dyes, 30 μL of PBS, IR-783 and IR-783-LP-TMTP1 NPs (1 mg mL^{-1}) were intratumoral injected into nude mice. The NIR-I fluorescence signals were recorded at 1 d, 3 d, 5 d and 7 d post-injection by a small animal imaging system under 745 nm laser irradiation. The trend of NIR fluorescence intensity of tumor site over time was recorded (Fig. SI 13A). Notably, when compared to IR-783-LP-TMTP1 NPs, the NIR fluorescence intensity of IR-783 diminished on the 5 th d and disappeared completely on the 7th d (Fig. SI 13B), which indicated that the IR-783-LP-TMTP1 NPs can stay in the cervical tumor for at least 7 days. It was attributed to the size of IR-783-LP-TMTP1 NPs, which makes it more inclined to accumulating in tumors via the enhanced permeability and retention (EPR) effect.

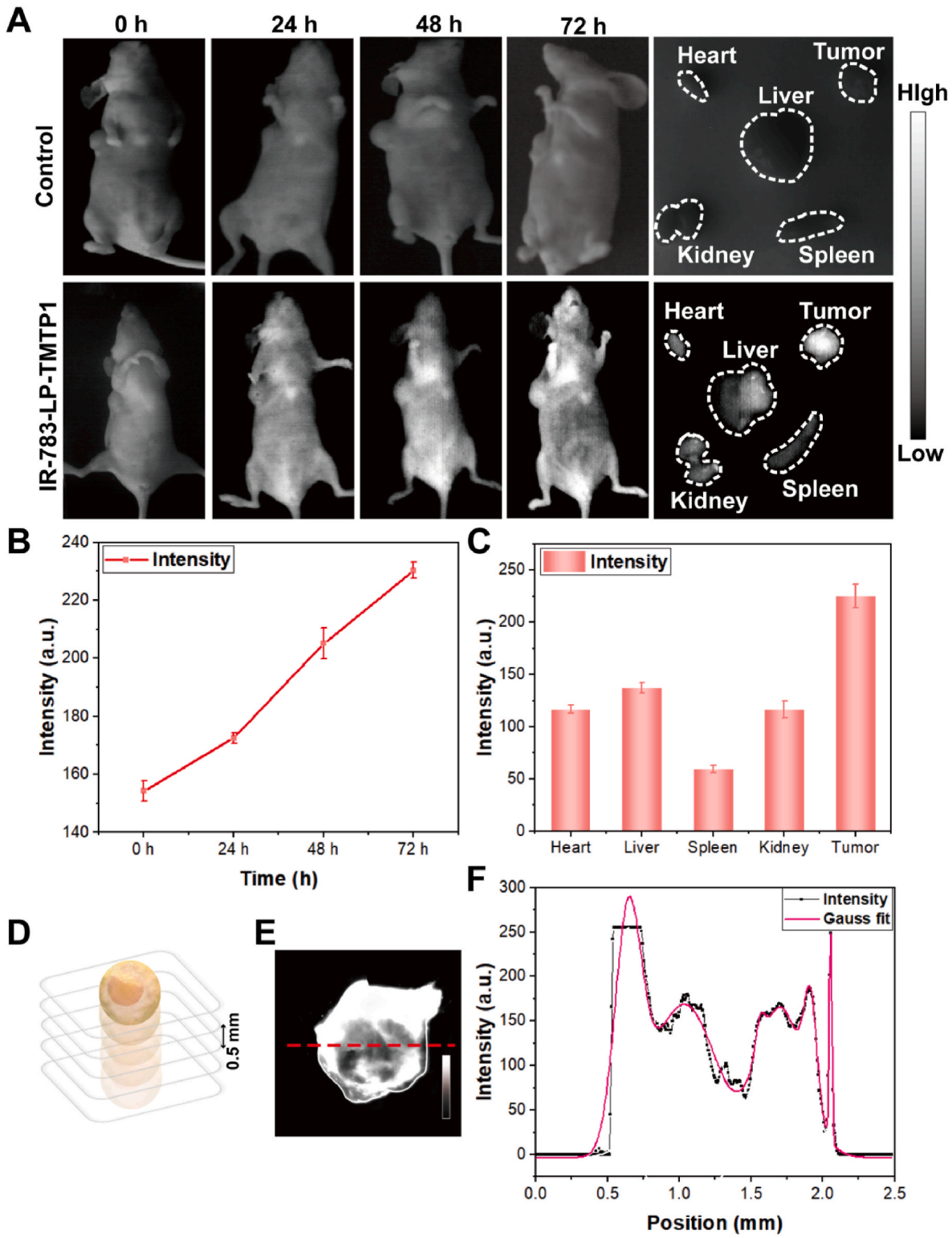

Fig. 5. *In vivo* molecular imaging and tumor targeting of IR-783-LP-TMTP1. (A) Images of a subcutaneous tumor-bearing mouse after tail-vein injection with PBS (200 μL) and IR-783-LP-TMTP1 (1 mg mL^{-1}, 200 μL)(Control group: PBS). Intensity of 808 Laser excitation: 30 mW cm^{-2}. (B) After injection of IR-783-LP-TMTP1, the fluorescence intensity on tumor at 0 h, 24 h, 48 h and 72 h. (C) The NIR-II fluorescence intensity of major organs and tumor. (D) Schematic diagram of tumor section. (E) NIR-II fluorescence image of tumor section. (F) The fluorescence intensity distribution of the tumor section.

Moreover, the stronger negative surface of IR-783-LP-TMTP1 NPs facilitates lymphatic enrichment. To evaluate this property, the 30 μL of PBS and IR-783-LP-TMTP1 NPs (0.5 mg mL^{-1}) were intramuscularly injected into the fore limb of female nude mice and imaged at various time points (0 h, 0.5 h, 11 d and 18 d) respectively. After 18 d, the mice were sacrificed and the SLN was collected for ex vivo NIR fluorescence imaging analysis. As shown in Fig. S14, the lymphatic enrichment characteristics of IR-783-LP-TMTP1 NPs were further confirmed. Thus, exploiting these characteristics of IR-783-LP-TMTP1 NPs, providing a novel strategy for long-term monitoring of tumor metastasis and

intraoperative SLN dissection. These results strongly suggest that the superior tumor EPR effect of IR-783-LP-TMTP1 NPs in cervical tumors, compared to other nanoparticles, can be attributed to the presence of TMTP1. TMTP1 plays a critical role in facilitating precise tumor targeting through its specific interaction with tumor microenvironment markers. This strategy not only enhances the efficacy of IR-783 but also holds significant potential for improving the tumor-targeting capabilities of other cyanine dyes with similar structures, such as ICG, IR-806, IR-820, FD-1080, and IRDye 800 CW. By leveraging the modular design of TMTP1, this approach could be extended to a wide range of imaging and therapeutic applications, offering a versatile platform for precision oncology. The findings highlight a promising pathway for the development of next-generation nanocarriers designed to overcome the limitations of traditional cyanine dyes, thereby advancing the field of tumor imaging and drug delivery.

4. Conclusions

In summary, we designed NIR-II emissive J-aggregates IR-783-LP-TMTP1 NPs with the combination of guanidine and IR-783, further demonstrating their superb fluorescence stability for NIR-II fluorescence imaging. The feature of this work lies in addressing the challenge of efficient biological imaging with cyanine molecules, and guanidine was employed to regulate the aggregation and arrangement of the cyanine dye IR-783. At the molecular level, the guanidine of TMTP1 NPs replaced Na^+ in IR-783, reducing the scissor opening angle and forming a near-coplanar structure. This near-coplanar structure facilitated the formation of J-aggregates with well brightness and better stability. At a higher morphological level, J-aggregates partially restricted intermolecular rotation, thereby enhancing fluorescence efficiency. Based on this strategy, structural adjustments at both the molecular (TMTP1 guanidine) and morphological (J-aggregates) levels led to the redshifted emission peaks of IR-783-LP-TMTP1 NPs compared to IR-783 and IR-783-LP NPs. Furthermore, IR-783-LP-TMTP1 NPs exhibited remarkable NIR-II fluorescence properties through NIR-II fluorescence microscopic imaging of blood vessels in the ear, brain, and legs of living mice. By enhancing the targeting ability of IR-783-LP-TMTP1 NPs, TMTP1 modification significantly increased the accumulation of IR-783 at cervical tumor sites. These results indicate that IR-783-LP-TMTP1 NPs offer an effective strategy for imaging-guided diagnosis and treatment of cervical cancer. The methodology and application of IR-783-LP-TMTP1 NPs can serve as a guide for molecules similar to IR-783, and inspire further development of cyanine dyes with ultralong emission wavelengths and high brightness.

CRediT authorship contribution statement

Jiaqi Zhou: Writing – review & editing, Writing – original draft, Visualization, Validation, Conceptualization. **Hao Li:** Writing – original draft, Methodology, Data curation. **Hui Li:** Formal analysis, Data curation. **Jiayi Ding:** Visualization, Supervision. **Zhong Du:** Formal analysis, Data curation. **Jiabao Xiong:** Validation, Supervision. **Hongyang Yao:** Visualization. **Xueliang Zhang:** Supervision. **Nuernisha Alifu:** Writing – review & editing, Writing – original draft, Funding acquisition, Formal analysis. **Biao Dong:** Writing – review & editing, Supervision, Conceptualization.

Declaration of competing interest

The authors declare that they have no known competing financial interests or personal relationships that could have appeared to influence the work reported in this paper.

Acknowledgements

J.Z. and H.L. contributed equally to this work. This work was supported by the Natural Science Foundation of Xinjiang Uygur Autonomous Region (2022D01C209), the National Natural Science Foundation of China (NSFC) under Grant (62035011, 82202220, 82060326, 52250007, and 82043475), State Key Laboratory of Pathogenesis, Prevention and treatment of High Incident Diseases in central Asia (SKL-HIDCA-2022-3 and SKL-HIDCA-2022-GJ1), the Xinjiang Uygur Autonomous Region Regional Collaborative Innovation Special Science and Technology Assistance Program (2022E02130), Xinjiang Uygur Autonomous Region Natural Science Foundation Key Project (2022D01D40) and Outstanding Youth Project (2023D01E06).

Appendix A. Supplementary data

Supplementary data to this article can be found online at https://doi.org/10.1016/j.mtbio.2025.101693.

Data availability

Data will be made available on request.

References

[1] F. Wang, Y. Zhong, O. Bruns, Y. Liang, H. Dai, *In vivo* NIR-II fluorescence imaging for biology and medicine, Nat. Photonics 18 (2024) 535–547.
[2] E.L. Schmidt, Z. Ou, E. Ximendes, H. Cui, C. Keck, D. Jaque, G. Hong, Near-infrared II fluorescence imaging, Nat. Rev. Methods Primers 4 (2024) 23.
[3] X. Luo, J. Shi, R. Wang, L. Cao, Y. Gao, J. Wang, M. Hong, X. Sun, Y. Zhang, Near-infrared persistent luminescence nanoprobe for early detection of atherosclerotic plaque, ACS Nano 8 (2024) 6500–6512.
[4] S. Song, Y. Wang, Y. Zhao, W. Huang, F. Zhang, S. Zhu, Q. Wu, S. Fu, B.Z. Tang, D. Wang, Molecular engineering of AIE luminogens for NIR-II/IIb bioimaging and surgical navigation of lymph nodes, Matter 5 (2022) 2847.
[5] C. Li, G. Chen, Y. Zhang, F. Wu, Q. Wang, Advanced fluorescence imaging technology in the near-infrared-II window for biomedical applications, J. Am. Chem. Soc. 142 (2020) 14789–14804.
[6] Y. Chen, S. Wang, F. Zhang, Near-infrared luminescence high-contrast *in vivo* biomedical imaging, Nat. Rev. Bioeng. 1 (2023) 60–78.
[7] L. Zhang, Y. Liu, Hai Huang, H. Xie, B. Zhang, W. Xia, B. Guo, Multifunctional nanotheranostics for near infrared optical imaging-guided treatment of brain tumors, Adv. Drug Deliv. Rev. 190 (2022) 114536.
[8] A. Smith, M. Mancini, S. Nie, Second window for in vivo imaging, Nat. Nanotechnol. 4 (2009) 710–711.
[9] K. Welsher, Z. Liu, S. Sherlock, J. Robinson, Z. Chen, D. Daranciang, H. Dai, A route to brightly fluorescent carbon nanotubes for near-infrared imaging in mice, Nat. Nanotechnol. 4 (2009) 773–780.
[10] J. Robinson, G. Hong, Y. Liang, B. Zhang, O. Yaghi, H. Dai, *In vivo* fluorescence imaging in the second near-infrared window with long circulating carbon nanotubes capable of ultrahigh tumor uptake, J. Am. Chem. Soc. 134 (2012) 10664–10669.
[11] S. Zhu, R. Tian, A. Antaris, X. Chen, H. Dai, Near-infrared-II molecular dyes for cancer imaging and surgery, Adv. Mater. 31 (2019) 1900321.
[12] X. Luan, H. Hu, Z. Sun, P. He, D. Zhu, Y. Xu, B. Liu, G. Wei, Assembling Ag2S quantum dots onto peptide nanosheet as a biomitetic two-dimensional nanoplatform for synergistic near infrared-II fluorescent imaging and photothermal therapy of tumor, J. Colloid Interface Sci. 663 (2024) 111–122.
[13] H. Yang, R. Li, Y. Zhang, M. Yu, Z. Wang, X. Liu, W. You, D. Tu, Z. Sun, R. Zhang, X. Chen, Q. Wang, Colloidal Alloyed quantum dots with enhanced photoluminescence quantum yield in the NIR-II window, J. Am. Chem. Soc. 143 (2021) 2601–2607.
[14] R. Tian, H. Ma, S. Zhu, J. Lau, R. Ma, Y. Liu, L. Lin, S. Chandra, S. Wang, X. Zhu, H. Deng, G. Niu, M. Zhang, A. Antaris, K. Hettie, B. Yang, Y. Liang, X. Chen, Multiplexed NIR-II probes for lymph node-invaded cancer detection and imaging-guided surgery, Adv. Mater. 32 (2020) 1907365.
[15] Z. Chen, B. Yun, Y. Hou, X. Wang, X. Wang, J. Xu, L. Jiang, T. Han, H. Zhang, F. Zhang, NIR-II anti-Stokes luminescence nanocrystals with 1710 nm excitation for in vivo bioimaging, Angew. Chem. Int. Ed. (2024), https://doi.org/10.1002/anie.202416893.
[16] J. Wu, Z. Chen, Y. Xie, Y. Fan, Advances in lanthanide-based NIR-IIb probes for in vivo biomedical imaging, Small Methods (2024), https://doi.org/10.1002/smtd.202401462.
[17] Y. Zhong, Z. Ma, F. Wang, X. Wang, H. Dai, *In vivo* molecular imaging for immunotherapy using ultra-bright near-infrared-IIb rare-earth nanoparticles, Nat. Biotechnol. 37 (2019) 1322–1331.
[18] L. Zhu, Z. Du, J. Xiong, H. Li, C. Zhang, X. Zhang, N. Alifu, B. Dong, Phototheranostic LPP-QDs-IR820 nanocomposites for specific NIR-II imaging of lymphatic and photothermal therapy of cervical tumors, Adv. Healthcare Mater. 13 (2024) 2401358.

[19] K. Wang, X. Wen, X. Chen, Y. Yue, Y. Yang, H. Zhu, M. Wang, H. Jiang, Promoting in vivo NIR-II fluorescent imaging for lipid in lipid metabolism diseases diagnosis, Anal. Chem. 5 (2024) 2264–2272.
[20] S. Ray, N. Bag, S. Bardhan, I. Hasan, B. Guo, Recent progress in NIR-II fluorescence imaging-guided drug delivery for cancer theranostics, Adv. Drug Deliv. Rev. 197 (2023) 114821.
[21] N. Zhu, J. Xu, Q. Su, T. Han, D. Zhou, Y. Zhang, S. Zhu, Site-specific albumin tagging with NIR-II fluorogenic dye for high-performance and super-stable biomiaging, Thno 14 (2024) 1860–1872.
[22] D. Hu, M. Zha, H. Zheng, D. Gao, Z. Sheng, Recent advances in indocyanine green-based probes for second near-infrared fluorescence imaging and therapy, Research 8 (2025) 583.
[23] E. Feng, Y. Liu, S. Lv, D. Liu, S. Huang, Z. Li, F. Song, Fine-Tuning Cu(II)-induced self-assembly of hydrophilic cyanine dyes for enhanced tumor photothermal therapy, Adv. Funct. Mater. 32 (2022) 2209258.
[24] X. Zhang, J. Gao, Y. Tang, J. Yu, S. Liew, C. Qiao, Y. Cao, G. Liu, H. Fan, Y. Xia, J. Tian, K. Pu, Z. Wang, Bioorthogonally activatable cyanine dye with torsion-induced disaggregation for *in vivo* tumor imaging, Nat. Commun. 13 (2022) 3513.
[25] Z. Hu, L. Feng, P. Yang, 2, 1, 3-Benzothiadiazole derivative small molecule fluorophores for NIR-II bioimaging, Adv. Funct. Mater. (2024), https://doi.org/10.1002/adfm.202310818.
[26] L. Li, X. Dong, J. Li, J. Wei, A short review on NIR-II organic small molecule dyes, Dyes Pigments 183 (2020) 108756.
[27] S. Usama, T. Thompsom, K. Burgess, Productive manipulation of cyanine dye pi-networks, Angew. Chem. 58 (2019) 8974–8976.
[28] S. Zhu, Z. Hu, R. Tian, B. Yung, Q. Yang, S. Zhao, D. Kiesewetter, G. Niu, H. Sun, A. Antaris, X. Chen, Repurposing cyanine NIR-I dyes accelerates clinical translation of near-infrared-II (NIR-II) bioimaging, Adv. Math. (2018) 1802546.
[29] Z. Lei, C. Sun, P. Pei, S. Wang, D. Li, X. Zhang, F. Zhang, Stable, wavelength-tunable fluorescent dyes in the NIR-II region for *in vivo* high-contrast bioimaging and multiplexed biosensing, Angew. Chem. 58 (2019) 201904182.
[30] M. Leito, D. Melo-Diogo, C. Alves, R. Lima-Sousa, I. Correia, Prototypic heptamethine cyanine incorporating nanomaterials for cancer phototheragnostic, Adv. Healthcare Mater. 9 (2020) 1901665.
[31] H. Huang, M. Li, J. Gu, S. Roy, J. Jin, T. Kuang, Y. Zhang, G. Hu, B. Guo, Bright NIR-II emissive cyanine dye-loaded lipoprotein-mimicking nanoparticles for fluorescence imaging-guided and targeted NIR-II photothermal therapy of subcutaneous glioblastoma, J. Nanobiotechnol. 22 (2024) 788.
[32] Z. Sheng, Y. Li, D. Hu, T. Min, D. Gao, J. Ni, P. Zhang, Y. Wang, X. Liu, K. Li, H. Zheng, B. Tang, Centimeter-deep NIR-II fluorescence imaging with nontoxic AIE probes in nonhuman primates, Research 2020 (2020) 4074593.
[33] C. Ou, Z. Zhao, L. An, L. Zheng, F. Gao, Q. Zhu, W. Wang, J. Shao, L. Xie, X. Dong, J-aggregate promoting NIR-II emission for fluorescence/photoacoustic imaging-guided phototherapy, Adv. Healthcare Mater. 13 (2024) 2400846.
[34] H. Piwonski, S. Nozue, H. Fujita, T. Michinobu, S. Habuchi, Organic J-aggregate nanodots with enhanced light absorption and near-unity fluorescence quantum yield, Nano Lett. 21 (2021) 2840–2847.
[35] X. Wang, Z. Jiang, Z. Liang, T. Wang, Y. Chen, Z. Liu, Discovery of BODIPY J-aggregates with absorption maxima beyond 1200 nm for biophotonics, Sci. Adv. 8 (2022) eadd5660.
[36] K. Lee, Y. Gao, W. Wei, J. Tan, Y. Wan, Z. Feng, Y. Zhang, Y. Liu, X. Zheng, C. Cao, H. Chen, P. Wang, S. Li, K. Wong, C. Lee, Anti-quenching NIR-II J-Aggregates of Benzo[c]thiophene fluorophore for highly efficient bioimaging and phototheranostics, Adv. Mater. 35 (2023) 2211632.
[37] C. Sun, B. Li, M. Zhao, S. Wang, Z. Lei, L. Lu, H. Zhang, L. Feng, C. Dou, D. Yin, H. Xu, Y. Cheng, F. Zhang, J-aggregates of cyanine dye for NIR-II in vivo dynamic vascular imaging beyongd 1500 nm, J. Am. Chem. Soc. 141 (2019) 19221–19225.
[38] X. Hu, C. Zhu, F. Sun, Z. Chen, J. Zou, X. Chen, Z. Yang, J-aggregation strategy toward potentiated NIR-II fluorescence bioimaging of molecular fluorophores, Adv. Mater. 36 (2024) 2304848.
[39] W. Chen, C. Cheng, E. Cosco, S. Ramakrishman, J. Lingg, O. Bruns, J. Zink, E. Sletten, Shortwave infrared imaging with J-aggregates stablilized in hollow mesoporous silica nanoparticles, J. Am. Chem. Soc. 141 (2019) 12475–12480.
[40] B. Du, R. Liu, C. Qu, K. Qian, Y. Suo, F. Wu, H. Chen, X. Li, Y. Li, H. Liu, Z. Cheng, J-aggregates albumin-based NIR-II fluorescent dye nanoparticles for cancer phototheranostics, Mater. Today Bio 16 (2022) 100366.
[41] Y. Li, T. Ma, H. Jiang, W. Li, D. Tian, J. Zhu, Z. Li, Anionic cyanine J-type aggregate nanoparticles with enhanced photosensitization for mitochondria-targeting tumor phototherapy, Angew. Chem. Int. Ed. 61 (2022) e202203093.
[42] R. Wei, G. Jiang, M. Lv, S. Tan, X. Wang, Y. Zhou, T. Cheng, X. Gao, X. Chen, W. Wang, C. Zou, F. Li, X. Ma, J. Hu, D. Ma, D. Luo, L. Xi, TMTP1-modified indocyanine green-loaded polymeric micelles for targeted imaging of cervical cancer and metastasis sentinel lymph node in vivo, Thno 9 (2019) 7325–7344.
[43] A. Becke, Density-functional thermochemistry. I. The Effect of the exchange-only gradient correction, J. Chem. Phys. 96 (1992) 2155–2160.
[44] S. Grimme, L. Goerigk, Effect of the damping function in dispersion corrected density functional theory, J. Comput. Chem. 32 (2011) 1456–1465.
[45] A. Mclean, G. Chandler, Contracted Gaussian basis sets for molecular calculations. I. Second row atoms, Z = 11-18, J. Chem. Phys. 72 (1980) 5639–5648.
[46] G. Scalmani, M. Frisch, Continuous surface charge polarizable continuum models of solvation. I. General formalism, J. Chem. Phys. 132 (2010) 114110.
[47] S. Choi, J. Bouffard, Y. Kim, Aggregation-induced emission enhancement of a mesotrifluoromethyl BODIPY *via* J-aggregation, Chem. Sci. 5 (2013) 751–755.
[48] X. Zeng, J. Long, S. Tian, G. Xiao, Random area pixel variation and random area transform for visible-infrared cross-modal pedestrian re-identification, Exp. Sys. with Appli. 215 (2023) 119307.
[49] B. Guo, Z. Feng, D. Hu, S. Xu, E. Middha, Y. Pan, C. Liu, H. Zheng, J. Qian, Z. Sheng, B. Liu, Precise deciphering of brain vasculatures and microscopic tumors with dual NIR-II fluorescence and photoacoustic imaging, Adv. Mater. 31 (2019) 1902504.
[50] Z. Feng, X. Yu, M. Jiang, L. Zhu, Y. Zhang, W. Yang, X. Wang, G. Li, J. Qian, Excretable IR-820 for in vivo NIR-II fluorescence cerebrovascular imaging and photothermal therapy of subcutaneous tumor, Thno 9 (2019) 5706–5719.
[51] G. Hong, J. Lee, J. Robinson, U. Raaz, L. Xie, N. Huang, J. Cooke, H. Dai, Multifunctional *in vivo* vascular imaging using near-infrared II fluorescence, Nat. Med. 18 (2012) 1841–1846.